Research Article

Non-corrosive and low-cost synthesis of hierarchically porous carbon frameworks for high-performance lithium-ion capacitors

Tong Qian [a], Yunchun Huang [a], Mengdi Zhang [a], Zhengzheng Xia [a], Haiyan Liu [b], Lu Guan [a], Han Hu [a, *], Mingbo Wu [a, **]

[a] State Key Laboratory of Heavy Oil Processing, College of Chemical Engineering, China University of Petroleum (East China), Qingdao, 266580, China
[b] New Energy Division, YanKuang Group Co. Ltd., Zoucheng, 273500, China

ARTICLE INFO

ABSTRACT

Because of their capability of rapid lithium uptake/release and robust capacitive energy storage, hierarchically porous carbon frameworks are widely regarded as promising electrode materials for lithium-ion capacitors. The current technologies for their syntheses involve either a heavily corrosive KOH activation or harsh template-removing processes exerting heavy environmental burdens. To surmount these drawbacks, we, herein, report the production of such an architecture by simply carbonizing petroleum asphalt with $KHCO_3$ contributing to hierarchically porous frameworks with high specific surface area in a non-corrosive condition. The microporous carbon nanosheets are curved to give mesopores and interconnected for macropores. Because of these structural merits, the rate-capable lithium storage is realized and the capacitive performance is three-times higher than that of widely used activated carbon cathodes. Furthermore, the lithium-ion capacitors simultaneously using these materials as the anode and cathode can deliver a high energy density of 112 Wh kg^{-1} at a power density of 260 W kg^- and present an energy density of 48 Wh kg^{-1} at a high-power density of 52 kW kg^{-1}. The versatile capabilities provided by the mild and low-cost carbon materials may find an alternative strategy for the real application of lithium-ion capacitors and other hybrid devices.

© 2020 Elsevier Ltd. All rights reserved.

1. Introduction

To reduce the heavy fossil fuel dependence, renewable energy sources, such as solar and wind power, have been largely deployed in the past decades [1]. In contrast to the traditional energy technologies, renewable energy is supplied intermittently and its efficient utilization requires high-performance energy storage devices [2–7]. Among them, lithium-ion batteries (LIBs) and supercapacitors (SCs) have deeply penetrated into our increasing electrified society for long-lasting use and power-demand application, respectively [8–11]. Nevertheless, many of the current and emerging applications put forward urgent needs for energy storage technologies simultaneously affording high energy density and power density, which are beyond the capability of the current technologies [12]. As a result, the exploration of energy storage systems that reconcile the merits of LIBs and SCs has been highly regarded as the research frontier of energy storage technologies [3,13–15].

Recently, lithium-ion capacitors (LICs) consisting of an anode of LIBs and capacitive cathode, have been proposed as a promising candidate to fulfill the increasing requirements on high-performance energy storage devices [16–21]. The anode of LICs operates using the lithium-ions involved bulk-phase reactions to secure high energy while the capacitive cathode facilitates the formation of the electrical double-layer for rate-capable output [13,22–25]. Typically, activated carbon (AC) is employed as the cathode material while hard carbon has been considered as the preferable choice of materials for the anode to reduce the kinetic gap between the two electrodes [26,27]. Nevertheless, both of the two electrode materials are quite expensive mainly because of the complicated synthesis procedure and corrosive production condition which largely restrict their popularization. For example, the ACs are generally produced by activation of the precursor with KOH at elevated temperatures that imposes extremely rigorous requirements on equipment [28]. In addition, the employment of a single type of materials for both the cathode and anode will be

appealing for further reducing the cost of the energy storage devices [29–31]. In this context, it is of paramount importance to cost-effectively produce a versatile material simultaneously serving as the cathode and anode for LICs.

Hierarchically porous carbon frameworks effectively organizing excellent electrical conductivity, large specific surface area, facilitated ion transportation paths, and abundant active sites are highly desired for rapid lithium uptake/release and large capacitive energy storage [18,19,32,33]. Their synthesis usually employs tedious and multi-step procedures. The replacement of the laborious processes with simple and cost-effective methods will essentially address the aforementioned drawbacks and promote the real application of LICs [13,34]. Herein, we report a facile synthesis of such an architecture by simply carbonizing the petroleum asphalt in the presence of $KHCO_3$, both of which are low-cost precursors. The $KHCO_3$ would decompose to K_2CO_3 to guide the formation of frameworks while the light fractions within the asphalt facilitate the creation of micro- and mesopores. Benefiting from the structural merits, a reversible lithium storage capacity of around 500 mA h g^{-1} is offered at a current density of 0.2 A g^{-1} and almost 50% of capacity is retained with a 25-fold increase of the current density. Meanwhile, a large specific capacity of 100 mA h g^{-1} is produced for reversible capacitive energy storage, which is 3 times higher than that of the traditional AC cathode. In particular, the LICs using this material as both cathode and anode can deliver a high energy density of 112 Wh kg^{-1} at a power density of 260 W kg^{-1} and a large power density of 52 kW kg^{-1} at an energy density of 48 Wh kg^{-1}. This work may offer an alternative avenue to construct high-performance LICs using low-cost and facilely synthesized hierarchically porous carbon frameworks.

2. Experimental section

2.1. Material synthesis

Petroleum asphalt provided by Sinopec Group was used as the carbon precursor. All other chemicals in the present work were of analytical grade and used without further purification. Typically, 1 g of petroleum asphalt and 4 g of potassium bicarbonate were grinded in an agate mortar for 10 min. Subsequently, the mixture was heated to 600–1000 °C with a ramping rate of 5 °C min^{-1} and held at this temperature for 2 h in a temperature-programmed tube furnace under a continuous nitrogen flow. After cooling down to room temperature, the obtained product was washed with deionized water to remove salts and collected by vacuum filtration, followed by drying at 60 °C for 24 h in a vacuum oven. The petroleum-asphalt-derived porous carbon nanosheets prepared at different temperatures were labeled as PCNs-T. The carbon yield of PCNs-T is shown in Table S1.

2.2. Material characterization

Scanning electron microscopy (SEM) images were obtained on a Hitachi S-4800. Transmission electron microscopy (TEM) and High resolution transmission electron microscope (HRTEM) images were collected on a JEM-2010 system at an accelerating voltage of 200 kV. X-ray diffraction (XRD) profiles of the carbon materials were evaluated using an X'Pert PRO MPD diffractometer with Cu Kα radiation (λ = 1.5406 Å). Raman spectra of the carbon materials at different temperatures were conducted on a Renishaw RM2000 employing a 512 nm laser. The Brunner–Emmet–Teller (BET) specific surface area and pore properties were obtained by analyzing the nitrogen sorption isotherms which were recorded using a Micromeritics ASAP 2020 analyzer. The surface chemistry and compositions of our samples were evaluated using an X-ray

photoelectron spectroscopy (XPS, Thermo Scientific Escalab 250XI) with Al Kα radiation. Thermogravimetric Analysis (TGA) was performed using a METTLER TGA 2.

2.3. Electrochemical measurements

The electrochemical performance was investigated using CR2032-type coin cells assembled in an argon-filled glovebox (H_2O < 0.1 ppm, O_2 < 0.1 ppm). The PCNs-T electrodes were prepared by a typical blade-coating process. The slurry composed of active materials (80 wt%), super P (10 wt%), and PVDF (10 wt%) was coated on Cu foil (Anode) and Al foil (Cathode), followed by drying in a vacuum oven at 80 °C for 12 h to produce the electrodes. The mass loading of PCNs-T was about 0.6–1.2 mg cm^2.

To evaluate the electrochemical performance of the anode and cathode, separately, the working electrode was paired with the lithium foil which simultaneously served as the counter and reference electrode to construct the coin-type half-cell. Microporous polypropylene film (Celgard 2400) was employed as the separator and 1 M $LiPF_6$ in EC, DMC and EMC (volume ratio of 1:1:1) was chosen as the electrolyte. The cathode and anode performances were evaluated in the potential range of 2.0–4.5 and 0–3.0 V vs Li/Li^+, respectively. The CV curves and Nyquist plots (100 kHz–10 mHz with an AC amplitude of 5 mV) were recorded using a CHI760D electrochemical working station while the GCD curves were detected on a Land CT2001A test system at various current densities.

For the device assembly, the anode was first pre-lithiated by cycling the electrode in a half cell at 0.1 A g^{-1} for 5 cycles and discharged to 0.1 V vs. Li/Li^+, which was then paired with the cathode to assemble a lithium ion capacitor (LIC).

The voltage window of the LIC was determined using a three-electrode system where lithium was introduced as the reference electrode in addition to the two working electrodes. The assembled LICs were galvanostatically charged and discharged on the CHI760D working station at various current densities in a voltage range from 1.0 to 4.2 V. The cyclic voltammetry (CV) measurements for the LICs were carried out on the CHI760D working station in a voltage range from 1.0 to 4.2 V. The cycling performance for the LIC was evaluated on the Land CT2001A test system. The current densities were determined based on the total mass of active materials on the anode and cathode. The specific energy density (E, Wh kg^{-1}) and power density (P, W kg^{-1}) were calculated based on the following equations:

$$P = \frac{I \times \Delta V}{m} \tag{1}$$

$$E = P \times t \tag{2}$$

$$\Delta V = \frac{V_{max} + V_{min}}{2} \tag{3}$$

where I is the discharge current (A), t is the discharge time (h), m is the total active materials in both electrodes (kg), and V_{max}(V) and V_{min}(V) are the maximum and minimum working voltage, respectively.

3. Results and discussion

3.1. Characterization and morphology

The simple and straightforward synthesis process for the PCNs-T is illustrated in Fig. 1. Firstly, petroleum asphalt and $KHCO_3$ are mixed by grinding, and the mixture shows a blocky morphology
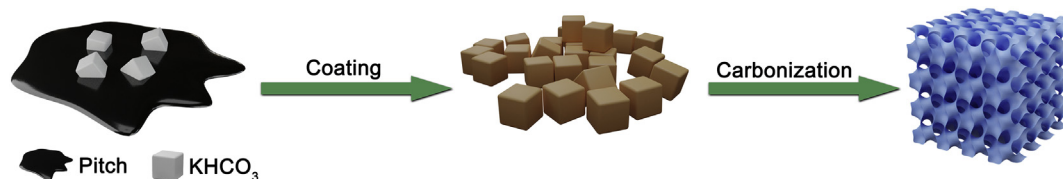
Fig. 1. Schematic illustration of the fabrication process of PCNs-T. (A colour version of this figure can be viewed online.)

(Fig. S1a). Thermogravimetric analysis (TGA) (Fig. S1b and Fig. S2a) was performed on the KHCO₃, petroleum asphalt and the mixture with a mass ratio of 1:4 between petroleum asphalt and KHCO₃ to illustrate the structural evolution of obtained porous carbon nanosheets (Fig. S1c). As shown in Fig. S1b, the initial weight loss at ~220 °C for the mixture is attributed to the complete decomposition of KHCO₃ into K₂CO₃, which is responsible for the formation of frameworks. The second weight loss at ~400 °C for the mixture is ascribed to the reaction of petroleum asphalt and K₂CO₃ during which the K₂CO₃ could be further degraded into CO₂ and other K-containing compounds to create micro- and mesopores [35,36]. The most widely used activation agent, namely KOH, may only contribute to the high porosity with negligible templating effects yet resulting in a highly corrosive condition. As shown in Fig. S2b

and Fig. 3a, the merely residual K₂CO₃ from the decomposed KHCO₃ could thoroughly be removed by washing with deionized water, preventing the use of any hazardous agents.

The typical structure synthesized at 800 °C was observed using the scanning electron microscopy (SEM) and transmission electron microscopy (TEM), as shown in Fig. 2. The low magnified SEM image (Fig. 2a) of the PCNs reveals a curved silk-like texture decorated with interconnected macropores which may facilitate efficient electrolyte transportation [37,38]. At higher magnifications (Fig. 2b), the surface of the PCNs offers the wrinkled and folded morphologies that contribute to rich mesopores [28]. These nanosheets are transparent to the electron beam under TEM observation (Fig. 2c and d), revealing their ultrathin thickness. The perpendicular edge in Fig. 2e provides a detailed thickness, which is
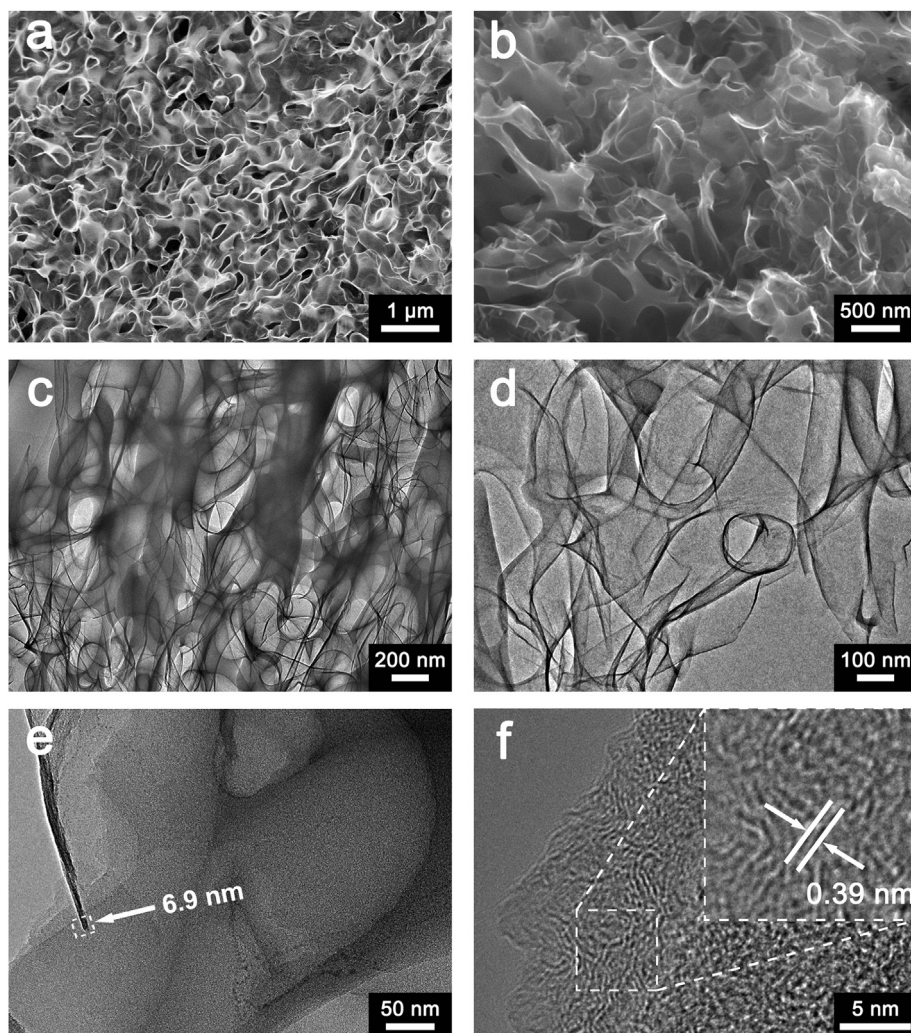

Fig. 2. Morphological characterization of PCNs-800: (a) and (b) SEM images. (c), (d), and (e) TEM images. (f) HRTEM image.
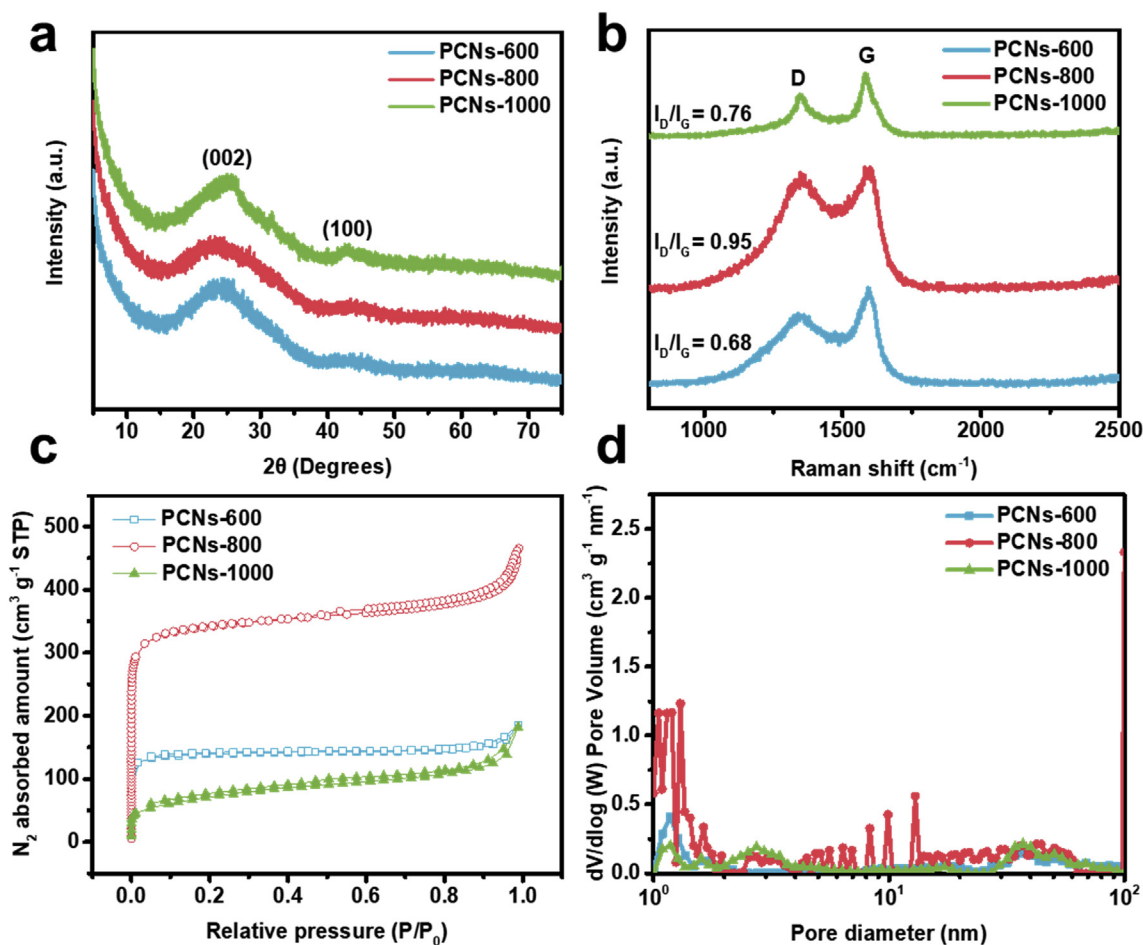
Fig. 3. (a) XRD patterns and (b) Raman curves of the PCNs-T. (c) N_2 sorption isotherm and (d) Pore size distribution of PCNs-T. (A colour version of this figure can be viewed online.)

determined to be around 6.9 nm. In the high-resolution TEM image (Fig. 2f), the surface of the PCNs shows quite a lot of micropores, confirming the hierarchical porosity. In addition, the lattice fringe is ordered in a short-range, indicative of an amorphous characteristic. Such structural merit may facilitate the lithium uptake/release that fundamentally enhances the rate capability of the anode [39]. The annealing temperature plays an important role in determining the structures of the as-obtained materials. When thermally treated at 600 °C, the as-obtained materials show a much thicker thickness (Fig. S3). When elevating the temperature to 1000 °C, collapse of the pore and cracking of carbon nanosheets would occur.

The structures of the as-prepared PCNs were further investigated using XRD, Raman spectra, Nitrogen sorption isotherms, and XPS methods. The XRD patterns of PCNs synthesized at different temperatures are compared in Fig. 3a. All of these samples only afford one broad diffraction peak implying their amorphous structures, which is good agreement with the TEM observation. The interlayer spacing is first increased and then decreased by ascending the heating temperature from 600 to 1000 °C, which is similar to the structural evolution of other asphalt-derived carbon materials [40]. The defect features of these materials are revealed in Raman spectra in Fig. 3b where the PCNs-800 exhibits the highest I_D/I_G ratio. Recent researches have unveiled the essential role of defects in carbon materials for energy storage and conversion which promote a significant interest in deliberately introducing defects in carbon materials for boosted performance [41,42]. As a result, our main attention has been concentrated on PCNs-800 with

rich defects. The XPS profile (Fig. S4) of PCNs-800 suggests a high carbon content and a minor amount of oxygen which mainly exists in the form of C-O, C=O, and O=C-O bonds. These bonds may contribute to pseudocapacitive energy storage facilitating a higher energy density [43]. Then, the specific surface area and porosity of PCNs-T were evaluated by using nitrogen-sorption isotherms as illustrated in Fig. 3c and d. The corresponding pore size distribution is based on DFT models. PCNs-600 and PCNs-1000 samples show the typical type I curve with predominant micropore structure. As for PCNs-800 sample, the rapid increase of N_2 adsorbed amount at the initial stage indicates the rich micropores while the partially separated adsorption and desorption branches at higher pressure suggest the presence of mesopores. Owing to distinctive pore structure, PCNs-800 shows the highest BET specific surface area up to 1316.9 m^2 g^{-1} and maximum total pore volume of 0.722 cm^3 g^{-1} compared to PCNs-600 and PCNs-1000 (For detailed information, see Table S1). All of these results are in good agreement with the SEM and TEM observations.

3.2. Electrochemical performance of PCNs-T anode

The lithium storage capability of hierarchically porous carbon frameworks was evaluated in a half cell with the PCNs-T as the working electrode and lithium foil as the reference and counter electrodes. The irreversible cathodic peak in the first cycle of the CV curves (Fig. 4a) indicates the formation of the solid electrolyte interphase (SEI) film while the subsequent cycles provide the
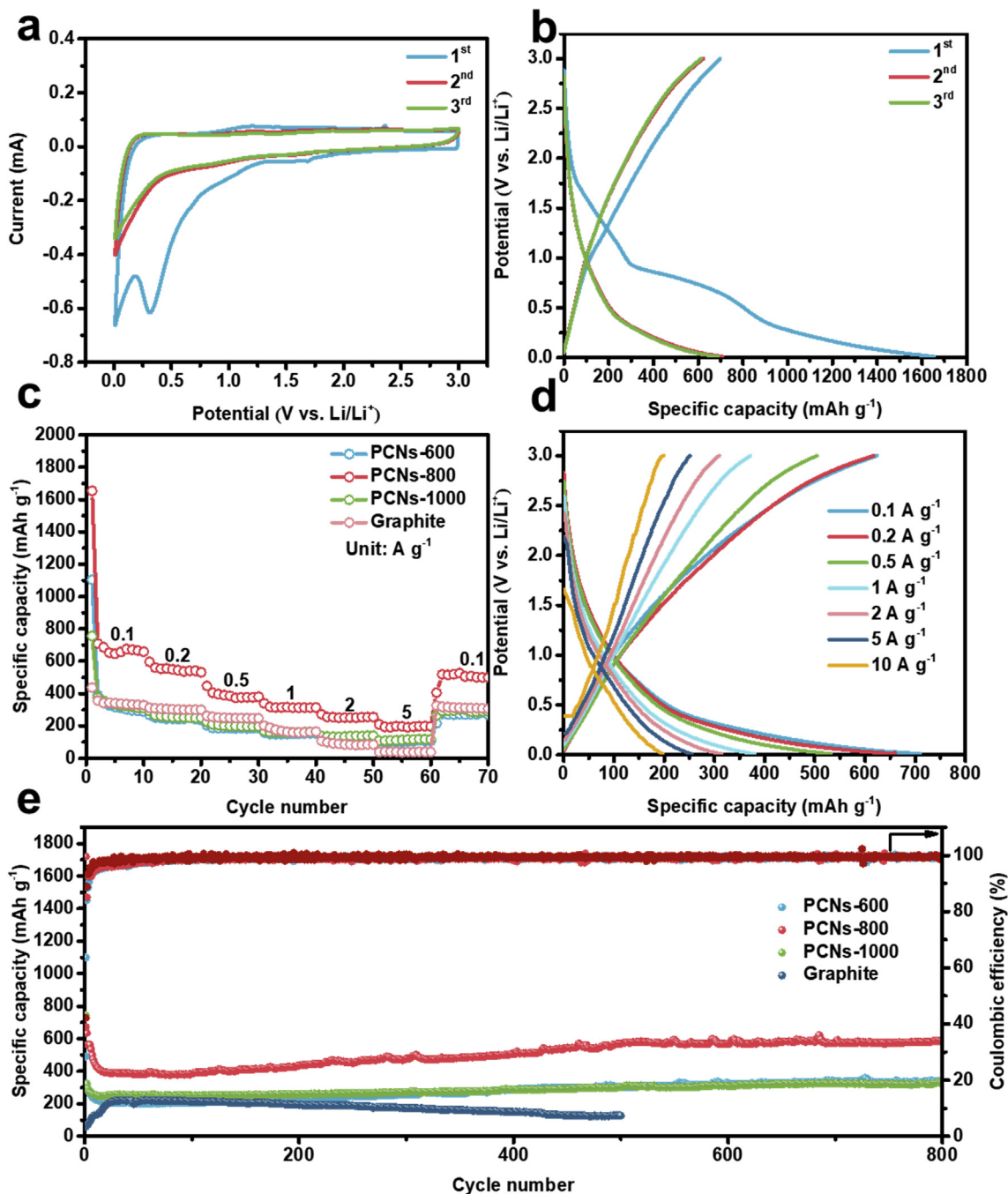
Fig. 4. Electrochemical properties of the PCNs-T electrode for lithium storage. (a) CV curves of PCNs-800 at 0.2 mV s^{-1}. (b) GCD profiles of PCNs-800 at 0.1 A g^{-1}. (c) Rate capability profiles for PCNs-T anodes. (d) GCD profiles of PCNs-800 anode at various current densities. (e) Cycling performance of PCNs-T and graphite anodes at 1 A g^{-1}. (A colour version of this figure can be viewed online.)

curves with a high degree of the rectangle shape, revealing that the lithium storage within this material is a surface-dominated process. The galvanostatic charge/discharge (GCD) curves of different cycles are exhibited in Fig. 4b and Fig. S5, giving slope profiles at a current density of 0.1 and 1 A g^{-1}. Besides, the PCNs-800 exhibits a relatively low initial coulombic efficiency (ICE) of 42.1% attributed to the irreversible decomposition of electrolyte, in accordance with the first CV cycle. Moreover, the GCD curves also suggest a surface-dominated process as there are no obvious plateaus in the GCD curves. To evaluate the explicit kinetic behavior of PCNs-800 for lithium storage, the power-law relationship was applied by

elaborately correlating the peak current (*i*) and the scan rate (*v*) in the CV curves at different scan rates using the following equation [44,45]:

$$i = av^b$$

Where *a* and *b* are adjustable parameters and the value of *b* is between 0.5 and 1. Generally, *b* value of 0.5 suggests a diffusion-controlled process while the *b* value of 1 reveals the completely surface-driven process. As shown in Fig. S6, the *b* value is much larger than 0.5, which is indicative of the high contribution of

surface-dominated process. The rate performance is evaluated by repeatedly discharging/charging at different current densities. By increasing the current density from 0.1 to 10 A g^{-1}, a high reversible capability of around 200 mA h g^{-1} is still maintained as shown in Fig. 4c. Then, the electrochemical performance of PCNs synthesized at different temperatures was compared in Fig. 4d where the capability of the graphite electrode is also illustrated. As shown, the reversible capacity of the PCNs-800 at the current densities of 0.1, 0.2, 0.5, 1.0, 2.0, and 5.0 A g^{-1} is around 709, 659, 532, 381, 314, and 255 mA h g^{-1}, respectively, which is far superior to graphite anode and the structures obtained at other temperatures. Then, these anodes were repeatedly discharged and charged for 800 cycles, and the retained specific capacity of PCNs-800 is 586 mA h g^{-1}, which is much higher than that of other anode materials. Furthermore, in order to achieve the optimal lithium storage, the various mass ratios between petroleum asphalt and KHCO$_3$ were researched. As shown in Fig. S7, the anode material derived from mass ratio of 1:4 shows the highest lithium storage capacity. As observed from the Nyquist plots of PCNs at different temperatures (Fig. S8), the PCNs-800 shows smaller resistance and faster charger transfer [44,46]. This superior performance may highlight the importance of structural defects for improved energy storage [47–49].

Due to the large specific surface area and high porosity, especially the hierarchical architecture, the PCNs-800 was further evaluated as the cathode of LICs. To investigate the electrochemical properties of the PCNs-800, a half-cell with PCNs-800 operated within the potential range of 2.0−4.5 V (vs. Li/Li$^+$) was assembled

and evaluated. Fig. 5a shows the CV curves of PCNs-800 at the scan rates ranging from 10 to 100 mV s^{-1}. Obviously, a relatively good rectangle shape is afforded at all of these scan rates, indicative of the excellent rate capability. All of the GCD curves exhibited in Fig. 5b and c at different current densities show relatively good symmetry and offer a specific capacity of 92, 85, 78, 75, 74, 69, and 66 mA h g^{-1} at the current densities of 0.1, 0.2, 0.5, 1.0, 2.0, 5.0, and 10.0 A g^{-1}, respectively, superior to that of the widely employed AC cathode. Moreover, the PCNs-800 cathode gives a depressed semicircle in the Nyquist plot (Fig. S9), underscoring the advantages of the hierarchical structure. The cyclic evaluation shown in Fig. 5d confirms excellent stability. All of these results reveal the promising potential of PCNs-800 for the cathode of LICs.

3.3. Full carbon symmetrical lithium-ion capacitors (PCNs-800// PCNs-800)

Due to the outstanding lithium storage performance and capacitive energy harvesting capability, the LICs were then assembled using the hierarchically porous carbon frameworks simultaneously as the anode and cathodes, as schematically illustrated in Fig. 6a. To explore the suitable mass ratio of cathode/anode, a lithium foil is involved as the reference electrode within the device (Fig. S10). As shown in Fig. 6b, the mass ratio of 1:1 allows the cathode and anode to work in a reasonable potential window, separately, and gives a large voltage window of around 3.2 V. Generally, the electrochemical performance of LICs is closely
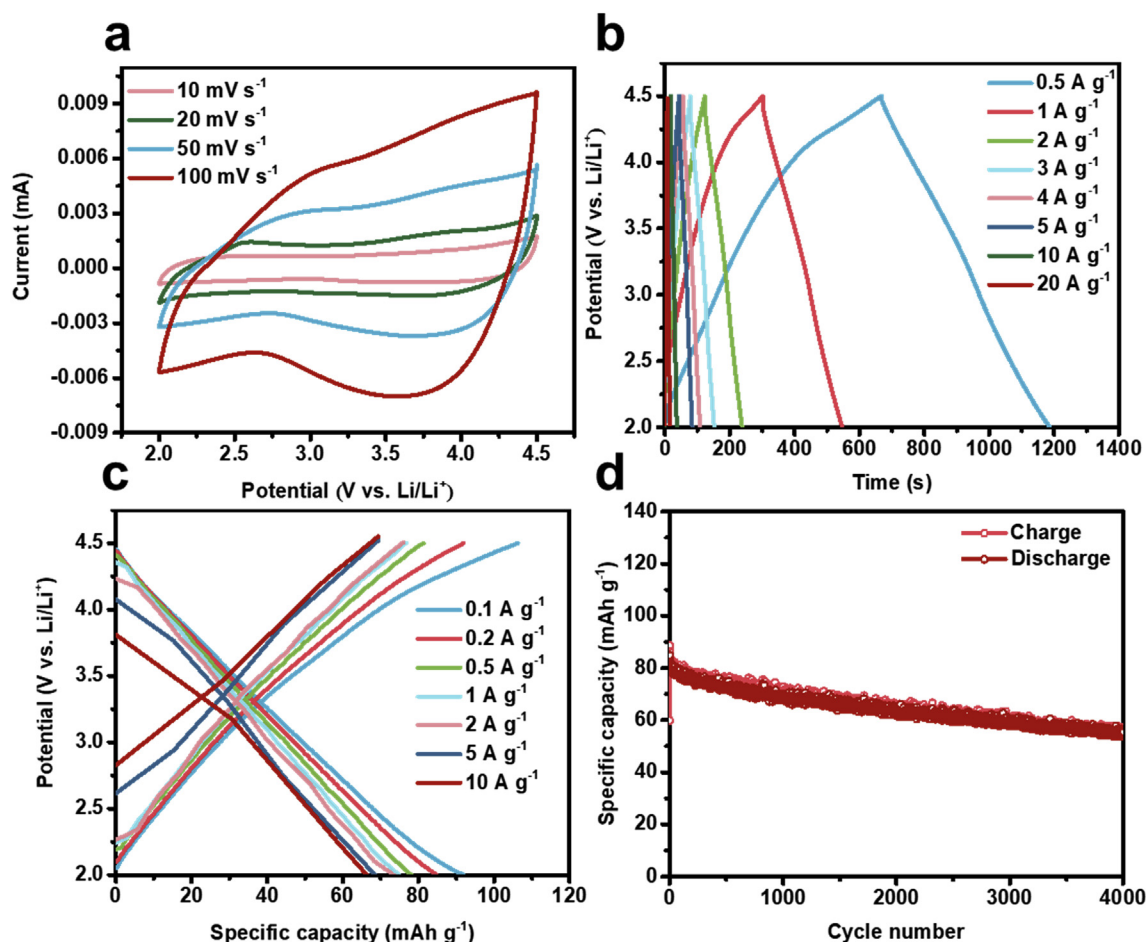

Fig. 5. (a) CV curves at different scan rates of PCNs-800 cathode. (b), (c) GCD profiles at different current densities for PCNs-800 cathode. (d) Cycling performance of PCNs-800 cathode at 2 A g^{-1}. (A colour version of this figure can be viewed online.)
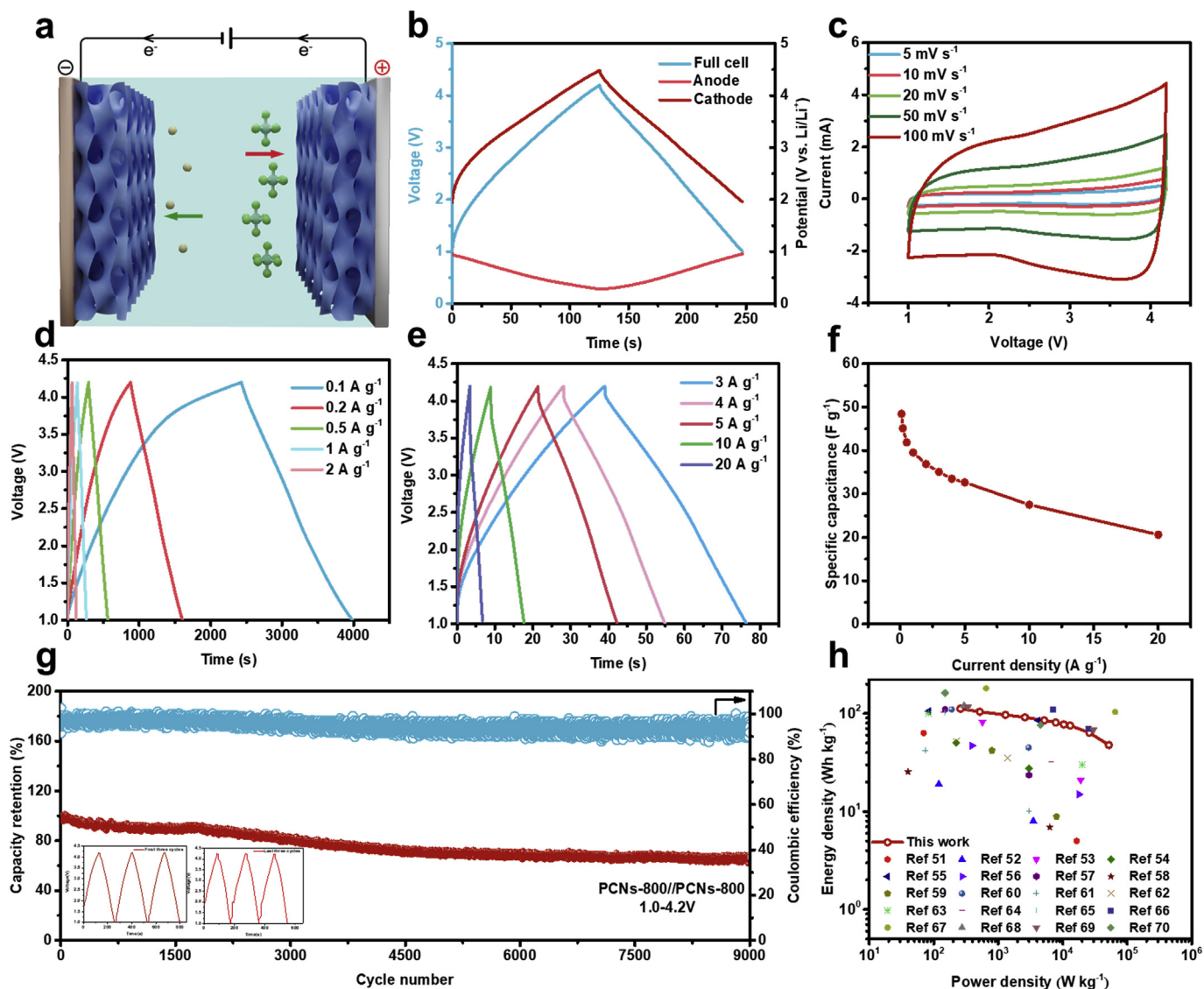
Fig. 6. Electrochemical performance of LICs using PCNs-800 as anode and cathode at a mass ratio of 1:1 (denoted as PCNs-800//PCNs-800). (a) Conceptual diagram of energy storage mechanism of LIC. (b) GCD profiles for the LIC system between 1.0 and 4.2 V and potential variation curves of the two electrodes at a current density of 1 A g^{-1}. (c) CV curves at different scan rates. (d) and (e) GCD profiles of LIC at different current densities. (f) Rate performance of the LIC at different current densities. (g) Cycling stability at 1 A g^{-1}. The inset is the GCD profiles of LIC for the first and last three cycles. (h) Ragone plots of the LIC. (A colour version of this figure can be viewed online.)

related to the operating potential of individual electrodes at different current densities. Appropriate potential range of anode and cathode plays a crucial role in determining the power density, energy density and cycling life of LICs. As shown in Fig. S11a, both of the lower limit potential (0.5 V) and the upper limit potential (1.4 V) of anode are comparatively high at a relatively small current density of 0.1 A g^{-1}, which results in a narrow potential range and an upper limit potential of cathode (high than 4.5 V), causing the poor capacity of LIC and irreversible decomposition of the electrolyte on the cathode side. With the increase of current density, the upper limit potential of anode decreases and the lower limit potential of anode increases. As shown in Fig. S11d, the potential range of anode from 0.3 to 1.0 V at a current density of 1 A g^{-1} ensures that the cathode was operated at such a wide and stable potential range of 2–4.5 V, which achieves maximize utilization of cathode capacity and thereby exhibits an admirable specific capacity and excellent cycling stability of LIC. Unfortunately, when the current density was further increased to 10 A g^{-1}, the potential range of anode was

0.6–1.0 V. On this condition, the upper limit potential of cathode exceeds 4.5 V, resulting in a rapid capacity decay of the entire system (Fig. S11g). As a consequence, the long cycling stability test was measured at optimal current density of 1.0 A g^{-1}. The electrochemical performance of LICs at same mass ratio between anode and cathode is superior to other devices with higher cathode mass loadings (Fig. S12). The relatively low mass loading on the cathode part is highly desirable for many high-performance energy storage devices [50]. In such a voltage window, the CV curves show excellent rectangle shapes in the scan rate from 5 to 100 mV s^{-1}, revealing the active mass on the cathode and anode is well matched. The GCD curves (Fig. 6d and e) further confirm the well-matched mass on both electrodes as the isosceles triangle-shaped profiles are maintained even by a 200-fold increase of the current density. Then, the rate performance is calculated based on these curves where the 42.6% of the capacitance is maintained with such an enormous increase of the current density, as illustrated in Fig. 6f. Based on above analysis, the cyclic performance was evaluated by

charging and discharging at a current density of 1.0 A g^{-1} for 9000 cycles. As shown in Fig. 6g, a relatively stable energy output is offered during the whole calendar life. To explore the practical performance of the as-assembled LICs, their energy density is plotted with the power density and compared with previous results in Fig. 6h. Such LICs display a high energy density of 112 Wh kg^{-1} at a low power density of 260 W kg^{-1} and present an energy density of 48 Wh kg^{-1} at a high-power density of 52 kW kg^{-1}, superior to most of the previously reported results. Such high energy and power density of PCNs-800//PCNs-800 device demonstrate a quite high level compared with previous reported LIC devices (Fig. 6g), such as Nb_2O_5/C//MSP-20 [51], $LiNi_{0.5}Mn_{1.5}O_4$//AC [52], TiO_2 NBA// Graphene hygrogel [53], $Li_4Ti_5O_{12}$//aCNF [54], Graphite//URGO [55], T-Nb_2O_5/Graphene paper//AC [56], Ti doped Nb_2O_5//PANI-CNT [57], CNT/V_2O_5//AC [58], TiO_2-RGO//AC [59], C//SnO_2-C [60], $CoMoS_4$// FCS [61], LTO/Graphene//AC [62], MnO/C//CNS [63], GC1100//SFAC-2 [64], MnNCN//AC [65], HC//AC [66], HCN-0//HCN-3 [67], HC//CS-AC [68], HCS//AC [69], NG//PJ-AC [70]. (For detailed information, see Table S2).

4. Conclusion

In summary, we propose a facile and cost-effective synthesis of hierarchically porous carbon frameworks using cheap precursors, namely petroleum asphalt and $KHCO_3$, in a non-corrosive condition. The rationally selected raw materials combined with the mild synthesis condition essentially reduce the cost of energy storage carbon materials. Moreover, the structural merits of the as-prepared materials, such as high conductivity, large specific surface area, and facilitated ion transportation path, permits rate-capable lithium storage and large capacitive energy harvesting. Then, such materials simultaneously served as the cathode and anode for LICs deliver the large energy density and high power density. Given the cheap precursors and simple fabrication, the hierarchically porous carbon frameworks produced in this work may hold great potential for a wealth of hybrid energy storage devices.

CRediT authorship contribution statement

Tong Qian: Methodology, Preparation, Data curation. **Yunchun Huang:** Preparation. **Mengdi Zhang:** Writing - review & editing. **Zhengzheng Xia:** Assistant in Preparation. **Haiyan Liu:** Discussion. **Lu Guan:** Characterization. **Han Hu:** Conceptualization, Writing - original draft. **Mingbo Wu:** Supervision.

Declaration of competing interest

The authors declare that they have no known competing financial interests or personal relationships that could have appeared to influence the work reported in this paper.

Acknowledgements

Appendix A. Supplementary data

Supplementary data to this article can be found online at https://doi.org/10.1016/j.carbon.2020.11.051.

References

[1] J.B. Goodenough, Energy storage materials: a perspective, Energy Storage Mater 1 (2015) 158–161.
[2] M. Armand, J.M. Tarascon, Building better batteries, Nature 451 (2008) 652–657.
[3] K. Naoi, S. Ishimoto, J.i. Miyamoto, W. Naoi, Second generation 'nanohybrid supercapacitor': evolution of capacitive energy storage devices, Energy Environ. Sci. 5 (2012) 9363–9373.
[4] Y.G. Patrice Simon, Bruce Dunn, Where do batteries end and supercapacitors begin? Science 343 (2014) 1210–1211.
[5] E. Pomerantseva, F. Bonaccorso, X. Feng, Y. Cui, Y. Gogotsi, Energy storage: the future enabled by nanomaterials, Science 366 (2019), eaan8285.
[6] J. Yang, X. Xiao, P. Chen, K. Zhu, K. Cheng, K. Ye, G. Wang, D. Cao, J. Yan, Creating oxygen-vacancies in MoO_{3-x} nanobelts toward high volumetric energy-density asymmetric supercapacitors with long lifespan, Nanomater. Energy 58 (2019) 455–465.
[7] J. Min, X. Wen, T. Tang, X. Chen, K. Huo, J. Gong, J. Azadmanjiri, C. He, E. Mijowska, A general approach towards carbonization of plastic waste into a well-designed 3D porous carbon framework for super lithium-ion batteries, Chem. Commun. 56 (2020) 9142–9145.
[8] P. Simon, Y. Gogotsi, Materials for electrochemical capacitors, Nat. Mater. 7 (2008) 845–854.
[9] B. Li, F. Dai, Q. Xiao, L. Yang, J. Shen, C. Zhang, M. Cai, Nitrogen-doped activated carbon for a high energy hybrid supercapacitor, Energy Environ. Sci. 9 (2016) 102–106.
[10] X. Yang, J. Mao, H. Niu, Q. Wang, K. Zhu, K. Ye, G. Wang, D. Cao, J. Yan, NiS_2/MoS_2 mixed phases with abundant active edge sites by sulfidation and graphene introduction towards high-rate supercapacitors, Chem. Eng. J. 406 (2021) 126713.
[11] X. Shi, S. Zhang, X. Chen, T. Tang, E. Mijowska, Three dimensional graphene/carbonized metal-organic frameworks based high-performance supercapacitor, Carbon 157 (2020) 55–63.
[12] B. Babu, P. Simon, A. Balducci, Fast charging materials for high power applications, Adv. Energy Mater. 10 (2020) 2001128.
[13] V. Aravindan, J. Gnanaraj, Y.S. Lee, S. Madhavi, Insertion-type electrodes for nonaqueous Li-ion capacitors, Chem. Rev. 114 (2014) 11619–11635.
[14] M. Salanne, B. Rotenberg, K. Naoi, K. Kaneko, P.L. Taberna, C.P. Grey, B. Dunn, P. Simon, Efficient storage mechanisms for building better supercapacitors, Nat. Energy 1 (2016) 16070.
[15] T. Zhang, F. Zhang, L. Zhang, Y. Lu, Y. Zhang, X. Yang, Y. Ma, Y. Huang, High energy density Li-ion capacitor assembled with all graphene-based electrodes, Carbon 92 (2015) 106–118.
[16] B. Li, F. Dai, Q. Xiao, L. Yang, J. Shen, C. Zhang, M. Cai, Activated carbon from biomass transfer for high-energy density lithium-ion supercapacitors, Adv. Energy Mater. 6 (2016) 1600802.
[17] P. Han, G. Xu, X. Han, J. Zhao, X. Zhou, G. Cui, Lithium ion capacitors in organic electrolyte system: Scientific problems, material development, and key technologies, Adv. Energy Mater. 8 (2018) 1801243.
[18] B. Li, J. Zheng, H. Zhang, L. Jin, D. Yang, H. Lv, C. Shen, A. Shellikeri, Y. Zheng, R. Gong, J.P. Zheng, C. Zhang, Electrode materials, electrolytes, and challenges in nonaqueous lithium-ion capacitors, Adv. Mater. 30 (2018) 1705670.
[19] A. Jagadale, X. Zhou, R. Xiong, D.P. Dubal, J. Xu, S. Yang, Lithium ion capacitors (LICs): development of the materials, Energy Storage Mater 19 (2019) 314–329.
[20] W. Fu, E. Zhao, R. Ma, Z. Sun, Y. Yang, M. Sevilla, A.B. Fuertes, A. Magasinski, G. Yushin, Anatase TiO_2 confined in carbon nanopores for high-energy Li-ion hybrid supercapacitors operating at high rates and subzero temperatures, Adv. Energy Mater. 10 (2019) 1902993.
[21] Y. Hao, S. Wang, Y. Shao, Y. Wu, S. Miao, High-energy density Li-ion capacitor with layered SnS_2/reduced graphene oxide anode and BCN nanosheet cathode, Adv. Energy Mater. 10 (2019) 1902836.
[22] S.M. Yanwu Zhu, Meryl D. Stoller, K.J. Ganesh, Weiwei Cai, Paulo J. Ferreira, Pirkle Adam, Robert M. Wallace, Katie A. Cychosz, Matthias Thommes, Su Dong, Eric A. Stach, Rodney S. Ruoff, Carbon-based supercapacitors produced by activation of graphene, Science 332 (2011) 1537–1541.
[23] Y. Zhai, Y. Dou, D. Zhao, P.F. Fulvio, R.T. Mayes, S. Dai, Carbon materials for chemical capacitive energy storage, Adv. Mater. 23 (2011) 4828–4850.
[24] Y. Ma, H. Chang, M. Zhang, Y. Chen, Graphene-based materials for lithium-ion hybrid supercapacitors, Adv. Mater. 27 (2015) 5296–5308.
[25] H. Wang, C. Zhu, D. Chao, Q. Yan, H.J. Fan, Nonaqueous hybrid lithium-ion and sodium-ion capacitors, Adv. Mater. 29 (2017) 1702093.
[26] L. Jin, J. Zheng, Q. Wu, A. Shellikeri, S. Yturriaga, R. Gong, J. Huang, J.P. Zheng, Exploiting a hybrid lithium ion power source with a high energy density over 30 Wh/kg, Mater, Today Energy 7 (2018) 51–57.
[27] L. Jin, X. Guo, R. Gong, J. Zheng, Z. Xiang, C. Zhang, J.P. Zheng, Target-oriented electrode constructions toward ultra-fast and ultra-stable all-graphene lithium ion capacitors, Energy Storage Mater 23 (2019) 409–417.

[28] X. Liu, C. Ma, J. Li, B. Zielinska, R.J. Kalenczuk, X. Chen, P.K. Chu, T. Tang, E. Mijowska, Biomass-derived robust three-dimensional porous carbon for high volumetric performance supercapacitors, J. Power Sources 412 (2019) 1–9.

[29] Q. Xia, H. Yang, M. Wang, M. Yang, Q. Guo, L. Wan, H. Xia, Y. Yu, High energy and high power lithium-ion capacitors based on boron and nitrogen dual-doped 3D carbon nanofibers as both cathode and anode, Adv. Energy Mater. 7 (2017) 1701336.

[30] F. Sun, X. Liu, H.B. Wu, L. Wang, J. Gao, H. Li, Y. Lu, In situ high-level nitrogen doping into carbon nanospheres and boosting of capacitive charge storage in both anode and cathode for a high-energy 4.5 V full-carbon lithium-ion capacitor, Nano Lett. 18 (2018) 3368–3376.

[31] Z. Li, L. Cao, W. Chen, Z. Huang, H. Liu, Mesh-like carbon nanosheets with high-level nitrogen doping for high-energy dual-carbon lithium-ion capacitors, Small 15 (2019) 1805173.

[32] C. Li, X. Zhang, K. Wang, X. Sun, Y. Ma, High-power and long-life lithium-ion capacitors constructed from N-doped hierarchical carbon nanolayer cathode and mesoporous graphene anode, Carbon 140 (2018) 237–248.

[33] J. Gong, X. Chen, T. Tang, Recent progress in controlled carbonization of (waste) polymers, Prog. Polym. Sci. 94 (2019) 1–32.

[34] J. Niu, R. Shao, M. Liu, J. Liang, Z. Zhang, M. Dou, Y. Huang, F. Wang, Porous carbon electrodes with battery-capacitive storage features for high performance Li-ion capacitors, Energy Storage Mater 12 (2018) 145–152.

[35] M. Zhou, Y. Lin, H. Xia, X. Wei, Y. Yao, X. Wang, Z. Wu, A molecular foaming and activation strategy to porous N-doped carbon foams for supercapacitors and CO_2 capture, Nano-Micro Lett. 12 (2020) 58.

[36] J. Deng, T. Xiong, F. Xu, M. Li, C. Han, Y. Gong, H. Wang, Y. Wang, Inspired by bread leavening: one-pot synthesis of hierarchically porous carbon for supercapacitors, Green Chem. 17 (2015) 4053–4060.

[37] Z.S. Wu, Y. Sun, Y.Z. Tan, S. Yang, X. Feng, K. Mullen, Three-dimensional graphene-based macro- and mesoporous frameworks for high-performance electrochemical capacitive energy storage, J. Am. Chem. Soc. 134 (2012) 19532–19535.

[38] P. Lu, Y. Sun, H. Xiang, X. Liang, Y. Yu, 3D amorphous carbon with controlled porous and disordered structures as a high-rate anode material for sodium-ion batteries, Adv. Energy Mater. 8 (2018) 1702434.

[39] H. Huang, R. Xu, Y. Feng, S. Zeng, Y. Jiang, H. Wang, W. Luo, Y. Yu, Sodium/potassium-ion batteries: boosting the rate capability and cycle life by combining morphology, defect and structure engineering, Adv. Mater. 32 (2020) 1904320.

[40] H. Hu, M. Wu, Heavy oil-derived carbon for energy storage applications, J. Mater. Chem. 8 (2020) 7066–7082.

[41] X. Yan, Y. Jia, X. Yao, Defects on carbons for electrocatalytic oxygen reduction, Chem. Soc. Rev. 47 (2018) 7628–7658.

[42] H. Hu, Q. Li, L. Li, X. Teng, Z. Feng, Y. Zhang, M. Wu, J. Qiu, Laser irradiation of electrode materials for energy storage and conversion, Matter 30 (2020) 95–126.

[43] N.R. Kim, S. Lee, M. Kim, H. Yoon, W. Hong, H.J. Jin, Y.S. Yun, Amphicharge-storable pyropolymers containing multitiered nanopores, Adv. Energy Mater. 7 (2017) 1700629.

[44] S. Fleischmann, J.B. Mitchell, R. Wang, C. Zhan, D.E. Jiang, V. Presser, V. Augustyn, Pseudocapacitance: from fundamental understanding to high power energy storage materials, Chem. Rev. 120 (2020) 6738–6782.

[45] C. Chen, Y. Huang, Z. Meng, M. Lu, Z. Xu, P. Liu, T. Li, N/O/P-rich three-dimensional carbon network for fast sodium storage, Carbon 170 (2020) 225–235.

[46] K.P. Lakshmi, K.J. Janas, M.M. Shaijumon, Antimony oxychloride/graphene aerogel composite as anode material for sodium and lithium ion batteries, Carbon 131 (2018) 86–93.

[47] R. Guo, C. Lv, W. Xu, J. Sun, Y. Zhu, X. Yang, J. Li, J. Sun, L. Zhang, D. Yang, Effect of intrinsic defects of carbon materials on the sodium storage performance, Adv. Energy Mater. 10 (2020) 1903652.

[48] Y. Dong, S. Zhang, X. Du, S. Hong, S. Zhao, Y. Chen, X. Chen, H. Song, Boosting the electrical double-layer capacitance of graphene by self-doped defects through ball-milling, Adv. Funct. Mater. 29 (2019) 1901127.

[49] L. Guan, H. Hu, L. Li, Y. Pan, Y. Zhu, Q. Li, H. Guo, K. Wang, Y. Huang, M. Zhang, Y. Yan, Z. Li, X. Teng, J. Yang, J. Xiao, Y. Zhang, X. Wang, M. Wu, Intrinsic defect-rich hierarchically porous carbon architectures enabling enhanced capture and catalytic conversion of polysulfides, ACS Nano 14 (2020) 6222–6231.

[50] J.S. Wei, C. Ding, P. Zhang, H. Ding, X.Q. Niu, Y.Y. Ma, C. Li, Y.G. Wang, H.M. Xiong, Robust negative electrode materials derived from carbon dots and porous hydrogels for high-performance hybrid supercapacitors, Adv. Mater. 31 (2019) 1806197.

[51] S.Y. Jinwoo Lee, Eunho Lim, Facile synthesis of Nb_2O_5@carbon core-shell nanocrystals with controlled crystalline structure for high-power anodes in hybrid supercapacitors, ACS Nano 9 (2015) 7497–7505.

[52] N. Arun, A. Jain, V. Aravindan, S. Jayaraman, W. Chui Ling, M.P. Srinivasan, S. Madhavi, Nanostructured spinel $LiNi_{0.5}Mn_{1.5}O_4$ as new insertion anode for advanced Li-ion capacitors with high power capability, Nanomater. Energy 12 (2015) 69–75.

[53] H. Wang, C. Guan, X. Wang, H.J. Fan, A high energy and power Li-ion capacitor based on a TiO_2 nanobelt array anode and a graphene hydrogel cathode, Small 11 (2015) 1470–1477.

[54] H. Xu, X. Hu, Y. Sun, W. Luo, C. Chen, Y. Liu, Y. Huang, Highly porous $Li_4Ti_5O_{12}$/C nanofibers for ultrafast electrochemical energy storage, Nanomater. Energy 10 (2014) 163–171.

[55] J.H. Lee, W.H. Shin, M.H. Ryou, J.K. Jin, J. Kim, J.W. Choi, Functionalized graphene for high performance lithium ion capacitors, ChemSusChem 5 (2012) 2328–2333.

[56] L.K. Donghui Long, Chuanfang Zhang, Free-standing T-Nb_2O_5/graphene composite papers with ultrahigh gravimetric/volumetric capacitance for Li-ion intercalation pseudocapacitor, ACS Nano 9 (2015) 11200–11208.

[57] X. Wang, P.S. Lee, Titanium doped niobium oxide for stable pseudocapacitive lithium ion storage and its application in 3 V non-aqueous supercapacitors, J. Mater. Chem. 3 (2015) 21706–21712.

[58] Z. Chen, V. Augustyn, J. Wen, Y. Zhang, M. Shen, B. Dunn, Y. Lu, High-performance supercapacitors based on intertwined CNT/V_2O_5 nanowire nanocomposites, Adv. Mater. 23 (2011) 791–795.

[59] H. Kim, M.-Y. Cho, M.-H. Kim, K.-Y. Park, H. Gwon, Y. Lee, K.C. Roh, K. Kang, A novel high-energy hybrid supercapacitor with an anatase TiO_2-reduced graphene oxide anode and an activated carbon cathode, Adv. Energy Mater. 3 (2013) 1500–1506.

[60] W.H. Qu, F. Han, A.H. Lu, C. Xing, M. Qiao, W.C. Li, Combination of a SnO_2−C hybrid anode and a tubular mesoporous carbon cathode in a high energy density non-aqueous lithium ion capacitor: preparation and characterisation, J. Mater. Chem. 2 (2014) 6549–6557.

[61] Y.K. Wang, W.B. Zhang, Y. Zhao, K. Li, L.B. Kong, Coprecipitation reaction system synthesis and lithium-ion capacitor energy storage application of the porous structural bimetallic sulfide $CoMoS_4$ nanoparticles, ACS Omega 3 (2018) 8803–8812.

[62] G. Wang, C. Lu, X. Zhang, B. Wan, H. Liu, M. Xia, H. Gou, G. Xin, J. Lian, Y. Zhang, Toward ultrafast lithium ion capacitors: a novel atomic layer deposition seeded preparation of $Li_4Ti_5O_{12}$/graphene anode, Nanomater. Energy 36 (2017) 46–57.

[63] Y. Zhao, Y. Cui, J. Shi, W. Liu, Z. Shi, S. Chen, X. Wang, H. Wang, Two-dimensional biomass-derived carbon nanosheets and MnO/carbon electrodes for high-performance Li-ion capacitors, J. Mater. Chem. 5 (2017) 15243–15252.

[64] Z. Yang, H. Guo, X. Li, Z. Wang, J. Wang, Y. Wang, Z. Yan, D. Zhang, Graphitic carbon balanced between high plateau capacity and high rate capability for lithium ion capacitors, J. Mater. Chem. 5 (2017) 15302–15309.

[65] C. Liu, C. Zhang, H. Fu, X. Nan, G. Cao, Exploiting high-performance anode through tuning the character of chemical bonds for Li-ion batteries and capacitors, Adv. Energy Mater. 7 (2017) 1601127.

[66] M. Arnaiz, V. Nair, S. Mitra, J. Ajuria, Furfuryl alcohol derived high-end carbons for ultrafast dual carbon lithium ion capacitors, Electrochim. Acta 304 (2019) 437–446.

[67] C. Li, X. Zhang, K. Wang, X. Sun, Y. Ma, High-power lithium-ion hybrid supercapacitor enabled by holey carbon nanolayers with targeted porosity, J. Power Sources 400 (2018) 468–477.

[68] S. Jayaraman, A. Jain, M. Ulaganathan, E. Edison, M.P. Srinivasan, R. Balasubramanian, V. Aravindan, S. Madhavi, Li-ion vs. Na-ion capacitors: a performance evaluation with coconut shell derived mesoporous carbon and natural plant based hard carbon, Chem. Eng. J. 316 (2017) 506–513.

[69] T. Panja, J. Ajuria, N. Diez, D. Bhattacharjya, E. Goikolea, D. Carriazo, Fabrication of high-performance dual carbon Li-ion hybrid capacitor: mass balancing approach to improve the energy-power density and cycle life, Sci. Rep. 10 (2020) 10842.

[70] P. Sennu, V. Aravindan, M. Ganesan, Y.G. Lee, Y.S. Lee, Biomass-derived electrode for next generation lithium-ion capacitors, ChemSusChem 9 (2016) 849–854.